

Interaction of a Pulsar Wind with the Expanding Supernova Remnant

Byung-Il Jun¹

Department of Astronomy, University of Minnesota, 116 Church Street, S.E., Minneapolis,
MN 55455

Received _____; accepted _____

¹current address : Lawrence Livermore National Laboratory, P.O. Box 808, L-630,
Livermore, CA 94551, email : jun2@llnl.gov

ABSTRACT

Recent HST (Hubble Space Telescope) observations of the Crab Nebula show filamentary structures that appear to originate from the Rayleigh-Taylor (R-T) instability operating on the supernova ejecta accelerated by the pulsar-driven wind. In order to understand the origin and formation of the filaments in the Crab Nebula, we study the interaction of a pulsar wind with the uniformly expanding supernova remnant by means of numerical simulation. We derive the self-similar solution of this model for a general power law density profile of supernova ejecta.

By performing two-dimensional numerical simulations, we find three independent instabilities in the interaction region between the pulsar wind and the expanding supernova remnant. The first weak instability occurs in the very beginning, and is caused by the impulsive acceleration of supernova ejecta by the pulsar wind. The second instability occurs in the post-shock flow (shock wave driven by pulsar bubble) during the intermediate stage. This second instability develops briefly while the gradients of density and pressure are of opposite signs (satisfying the criterion of the R-T instability). The third and most important instability develops as the shock driven by the pulsar bubble becomes accelerated ($r \propto t^{6/5}$). This is the strongest instability and produces pronounced filamentary structures that resemble the observed filaments in the Crab Nebula. Our numerical simulations can reproduce important observational features of the Crab Nebula. The high density heads in the R-T finger tips are produced because of the compressibility of the gas. The density of these heads is found to be about 10 times higher than other regions in the fingers. The mass contained in the R-T fingers is found to be 60% – 75% of the total shocked mass and the kinetic energy within the R-T fingers is 55% – 72% of the total

kinetic energy of the shocked flow. The R-T fingers are found to accelerate with a slower rate than the shock front, which is consistent with the observations. By comparing our simulations and the observations, we infer that the some finger-like filaments (region F or G in Hester’s observation) started to develop about 657 years ago.

Subject headings: hydrodynamics – instabilities – shock waves – pulsars – supernova remnants

1. Introduction

Pulsars release their rotational energy in the forms of a relativistic wind and electromagnetic waves (Rees and Gunn 1974) and this energy generates the nebula that expands into the surrounding supernova remnant. In the Crab Nebula, this spin-down power of pulsar is sufficient to support the synchrotron radiation of the nebula, although the complete model to link the pulsar to the nebula is yet to be given. The pulsar wind is also expected to interact with the expanding supernova remnant and produce some interesting observational results.

The study of the interaction between the pulsar wind and the enveloping supernova ejecta has been motivated since the recent observation of the Crab Nebula by the Hubble Space Telescope (HST) revealed the detailed morphology and ionization structures of the helium-rich filaments. The complex emission-line filaments would appear to originate from the Rayleigh-Taylor (R-T) instability operating on the ejecta accelerated by the pulsar wind (Hester et al. 1996). These finger-like structures seem to grow inward (toward the center of the remnant) and to be connected to each other at their origins by a faint, thin tangential structure (the “skin”). Some of the long finger-like structures terminate in dense “head” regions. The interface between the synchrotron nebula and an ejecta shell has been thought to be R-T unstable (Chevalier and Gull 1975; Chevalier 1977) since motions of the filaments (Trimble 1968) and the synchrotron nebula itself (Bietenholtz et al. 1991) revealed their outward post-explosion acceleration. The magnetic field in the Crab has been inferred to be strong (a few hundred μG) and seems to play an important role in the formation of the filaments. Polarimetric VLA observations of the Crab show a radially aligned magnetic field orientation (Bietenholz and Kronberg 1990), although the rotating pulsar is likely to produce toroidal (tangential) magnetic fields (Rees and Gunn 1974). The radial magnetic field can be produced as R-T fingers stretch the existing field lines.

In the Crab Nebula, the observed mass and kinetic energy are much smaller than expected from the typical supernova (see review by Davidson and Fesen 1985). Several authors have proposed that the Crab formed from a normal Type-II supernova remnant and that an outer fast-moving shell contains most of mass and kinetic energy (Chevalier 1977, Kennel and Coroniti 1984), despite the absence of convincing detection of the surrounding shell (e.g. Frail et al. 1995). In this model for the Crab, the pulsar wind pushes into the uniformly expanding supernova ejecta. Therefore, the model includes four shocks from the outside inward : a supernova blast wave, a reverse shock moving into the supernova ejecta, an outward facing shock wave driven by expanding pulsar bubble, and a wind termination shock (Fig.1). Note that the forward shock front driven by the pulsar bubble is actually disturbed by the instability (see Fig.5). The signature of the shock front driven by the pulsar bubble has been found near the boundary of the Crab Nebula recently by Sankrit and Hester (1997) although the existence of the shock is debated, because the steepening of the radio spectral index near the outer boundary of the Crab Nebula has not been found (Frail et al. 1995; Bietenholtz et al. 1997). Sankrit and Hester find that the shock should be expanding with a velocity about $v = 150 km/sec$ into the freely-expanding supernova ejecta.

The normal Type-II supernova remnant model is particularly attractive because there is no need for a peculiar low-energy supernova event and it can be applied to other pulsar-powered remnants. Also, the mechanism for the observed acceleration is naturally explained, because the pulsar’s wind shock expands with the law $r \propto t^{6/5}$ in the self-similar stage if the pulsar’s luminosity is assumed to be constant (Chevalier 1977). In fact, the low-energy event model itself, which is considered because of the discouraging observational results on the absence of fast moving shell in the Crab Nebula, has many problems to reconcile the observed features of the Crab Nebula. First, even low-energy supernova should produce an outer shock since the supersonically moving gas generates a shock ahead

of it. This shock should have a current expanding velocity, about $v_{shock} \sim 1400 km/sec$. Therefore, the fact that no steepening of the spectral index near the boundary of the Crab Nebula has been found cannot support the low-energy event model. Actually, this low energy event model can generate a stronger shock than that of normal type-II supernova model. Second, the acceleration of both the line-emitting filaments and synchrotron nebula and the well-resolved Rayleigh-Taylor finger-like filaments pointing inward have not been explained by the low-energy event model. Currently, the only mechanism that can accelerate both the synchrotron nebula and the filaments is the pulsar wind blowing into the freely-expanding supernova ejecta around the Crab Nebula.

In this paper, we will present the results of our numerical investigation of a Type-II supernova remnant model on the origin of the filamentary structures in the Crab Nebula. In §2, we study the self-similar solution for our model. In §3, our numerical methods and initial condition for the simulation is described. §4 presents our numerical results on the hydrodynamic evolution and fluid instabilities of the interaction region. In §5, we will discuss the evolution of Rayleigh-Taylor fingers in terms of mass and kinetic energy. We discuss the related issues to the Crab Nebula further in §6 and summarize our main conclusions in §7.

2. Self-Similar Solution

Chevalier(1977; 1984) has studied the self-similar solution for the current model of the pulsar bubble expanding into a uniformly moving medium of constant density. In order to understand the dynamics of the system and our numerical results, we generalize Chevalier’s self-similar solution for a power law density medium. We only consider the region between the contact discontinuity and the forward shock driven by the pulsar bubble. Using dimensional analysis, the expansion law can be obtained readily, $r \propto t^{\frac{6-n-l}{5-n}}$ where n and l

are the power law indices for the moving ejecta density ($\rho \propto r^{-n}$) and the pulsar luminosity ($L \propto t^{-l}$). For a constant pulsar luminosity and uniform ejecta density, the bubble expands with the law, $r \propto t^{1.2}$; that is accelerating. It should be noted that the solution is only applicable for $n < 3$ because of the finite mass requirement ($M \propto \frac{t^{n-3}r^{3-n}}{(3-n)}$) as pointed out by Chevalier (1992). Also, the bubble must expand at least with constant velocity (no deceleration is allowed) because the surrounding medium is freely expanding. In actual evolution, the bubble can decelerate at early stages while the bubble velocity is much higher than the ejecta velocity, because the medium motion can be negligible (see one-dimensional numerical result in section 4). However, as the bubble expansion approaches the self-similar stage, the effect of the moving medium is not negligible and the bubble expansion cannot decelerate. Therefore, the self-similar solution is only applicable for $l \leq 1$.

In order to derive a self-similar solution for general power law density profile of supernova ejecta, we can define the similarity variables

$$\zeta = \frac{r}{At^a} \quad (1)$$

$$\rho = t^{b-na}D(\zeta) \quad (2)$$

$$v = aAt^{a-1}V(\zeta) \quad (3)$$

$$p = a^2A^2t^{b-na+2a-2}P(\zeta) \quad (4)$$

where A is constant, $a = \frac{6-n-l}{5-n}$, and b is an expansion factor defined as $b = n - 3$. The expansion factor b is 0 if the surrounding medium is at rest. The effect of a constant expansion of the supernova ejecta is to change the density with the law $\rho \propto t^{n-3}$ at the same radius.

The one-dimensional fluid equations for a spherical coordinate system are

$$\frac{\partial \rho}{\partial t} + v \frac{\partial \rho}{\partial r} + \rho \frac{\partial v}{\partial r} + \frac{2\rho v}{r} = 0 \quad (5)$$

$$\frac{\partial v}{\partial t} + v \frac{\partial v}{\partial r} + \frac{1}{\rho} \frac{\partial p}{\partial r} = 0 \quad (6)$$

$$\frac{\partial p}{\partial t} + v \frac{\partial p}{\partial r} + \gamma p \frac{\partial v}{\partial r} + \frac{2\gamma p v}{r} = 0 \quad (7)$$

where γ is the adiabatic index.

Using the similarity variables, we can transform the fluid equations into the ordinary differential equations

$$\left(\frac{b}{a} - n + \frac{2V}{\zeta}\right)D + (V - \zeta)\frac{dD}{d\zeta} + D\frac{dV}{d\zeta} = 0 \quad (8)$$

$$\frac{(a-1)}{a}V + (V - \zeta)\frac{dV}{d\zeta} + \frac{1}{D}\frac{dP}{d\zeta} = 0 \quad (9)$$

$$\left(\frac{b-2}{a} - n + 2 + \frac{2\gamma V}{\zeta}\right)P + (V - \zeta)\frac{dP}{d\zeta} + \gamma P\frac{dV}{d\zeta} = 0. \quad (10)$$

These equations can be integrated from the shock front (driven by the expanding bubble) using the following boundary conditions

$$D(1) = \frac{\gamma+1}{\gamma-1} \quad (11)$$

$$V(1) = 1 + \frac{\gamma-1}{\gamma+1}(c-1) \quad (12)$$

$$P(1) = \frac{2}{\gamma+1}(1-c)^2 \quad (13)$$

where c is $\frac{1}{a}$ for a moving medium and 0 for a stationary medium.

Self-similar solutions for several different cases are shown in Fig.2. Adiabatic index is chosen to be 5/3 except for Fig.2d because the shocked supernova ejecta region is considered to be nonrelativistic while the pulsar wind is relativistic. Each plot shows density, gas pressure, and velocity profiles in the region between the contact discontinuity and the shock front. In general, the flow within the shell (shocked supernova ejecta) are found to be stable under the Rayleigh-Taylor instability criterion in all cases since the gas pressure gradient has the same sign as the density gradient. But the contact discontinuity

is Rayleigh-Taylor unstable for $a > 1$ because the shell is denser than the region inside of the contact discontinuity. Fig.2a is the case III in Chevalier (1984). The shell thickness is about $0.02r_{shock}$. Comparing Figs. 2a, 2b, and 2c, the shell becomes thicker as a increases as also found by Chevalier (1984). We find that the case in Fig.2b shows a thicker shell than the case for $a = 1.5, n = 0$. Fig.2d shows the same case as Fig.2a except for $\gamma = 1.1$. This case is considered to see the effect of radiative cooling. As expected, the shell is found to be thinner in the case for $\gamma = 1.1$ than $\gamma = 5/3$.

3. Numerical Methods and Initial Condition

Understanding the dynamical interaction between the pulsar wind and the ejecta requires multidimensional numerical simulations with high resolution because the development of the instability is highly nonlinear. High resolution simulations are particularly necessary to resolve the thin shell and small regions containing R-T fingers. For this problem, we utilize the ZEUS-3D code, developed and tested at the National Center for Supercomputing Application (Clarke & Norman, 1994). ZEUS-3D is a three-dimensional Eulerian finite difference code for solving the ideal MHD equations. The grid velocity is also allowed to change every timestep so that the grid can follow the expanding system. This is necessary in modeling the Crab Nebula in order to follow the expanding supernova remnant accurately and keep adequately high resolution at the interaction region between the pulsar wind and the supernova ejecta. For the detailed numerical algorithms of this code, readers are referred to Stone & Norman (1992).

The model includes the pulsar wind, moving supernova ejecta, and supernova shell confined by the supernova blast wave and reverse shock. Since we are interested in the interaction region between the pulsar wind and the supernova ejecta, our simulation excludes the supernova shell. Readers are referred to Jun & Norman (1996a; 1996b) for

detailed study of the dynamics of supernova shell. The pulsar wind is generated by the constant mechanical luminosity, $L = 1.0 \times 10^{40} \text{ergs/sec}$. The luminosity of the pulsar is given by $L = 2.0 \times \pi r^2 \rho v^3$ where r , ρ , v are the initial radius of the wind, the density of the wind gas, and the initial wind velocity, respectively. This luminosity is much higher than the current luminosity of the Crab pulsar, $L \sim 1.0 \times 10^{38} \text{ergs/sec}$, and is determined by accounting for the observed rate of decrease in the luminosity. The initial radius of the wind is chosen to be 0.1pc and the density of the pulsar wind gas is assumed to be $\rho = 1.67 \times 10^{-24} \text{gm/cc}$. The initial wind velocity is determined from the given luminosity accordingly. The supernova ejecta is initialized to be uniformly moving with $v = 500 \text{km/s}$ at 0.1pc , and the velocity at larger radius is linearly proportional to the radius. The density profile of the supernova ejecta is usually modeled by a constant density in inner core region and the power law density profile ($\rho \propto r^{-n}$) in the outer region although the mass ratio between two regions can change depending on the model. According to Chevalier & Fransson (1992), the forward shock driven by the pulsar bubble is likely to be still in the inner core region during the constant luminosity phase. In our simulation, we assume the constant density of supernova ejecta to be $\rho = 1.67 \times 10^{-22} \text{gm/cc}$ over the entire ejecta. Note that the ejecta density decreases with time because of ejecta expansion. We assume the entire fluid to be nonrelativistic gas with $\gamma = 5/3$, for simplicity. We defer a more general simulation with varying luminosity and different density profile of the ejecta including detailed physics such as magnetic field and cooling to a future project. Because of our idealized simple initial condition, we do not attempt to compare the evolution with exact time scale to the Crab Nebula. We focus our investigation on the development and the formation of the filamentary structures by fluid instabilities.

The simulation is carried out in a spherical coordinate system with the resolution 800×500 in the $r - \phi$ plane. The thin shell is resolved by about 16 grid cells in the r -direction with this mesh size, because the thickness of the thin shell is approximately 0.02 times the

shock radius. This resolution in the shell remains same throughout the evolution because grids are expanding as the forward shock moves out. We update the outer boundary condition in the r -direction to take into account the condition of the moving supernova ejecta in every time step. The boundary conditions in the ϕ – *direction* are assumed to be periodic. The density field is perturbed with the amplitude of 1% in the entire region. Incoming flow from the outer r boundary also includes the density perturbation in order to trigger the instability within the postshock flow (see next section for the instability). We evolve a Lagrangian invariant passive quantity (mass fraction function) to follow the contact discontinuity between the supernova ejecta and the pulsar wind. The mass fractions are assigned to be 0.0 in the pulsar wind and 1.0 in the supernova ejecta.

4. Hydrodynamic Evolution and Instabilities

4.1. One-Dimensional Results

First, The global evolution of the flow is studied by one-dimensional numerical simulations (Fig.3). In the early stage, the shock wave driven by the expanding pulsar bubble propagates much faster than the moving supernova ejecta and the density of supernova ejecta can be considered to be roughly constant (stationary medium stage). Figure 3a plots density, velocity, and gas pressure, from top panel to bottom panel at $t = 100$ years. Three typical hydrodynamical features; namely, a wind termination shock (W.T.), a contact discontinuity (C.D.) between the wind bubble and the shocked ambient medium, and a forward shock (F.S.) driven by pulsar bubble are clearly seen from inside outward. These flow structures resemble the wind solution in a stationary medium as described by Weaver et al. (1977). The shock expansion can be approximated as $r_{shock} \propto t^{3/5}$. As the shock velocity decreases and becomes comparable to the ejecta velocity, the ejecta can be no longer considered as a stationary medium and the effect of decreasing density of the ejecta

becomes important (moving medium stage). Then the shock accelerates and enters the self-similar stage which is described by $\rho_{ejecta} \propto t^{-3}$ and $r_{shock} \propto t^{6/5}$ (Chevalier 1977,1984). This stage is illustrated in Figure 3c. Figure 3b shows the intermediate stage evolving from the stationary medium stage to the moving medium stage. One noticeable feature is the thickness of the shell between the contact discontinuity and the forward shock. This shell thickness decreases with time and becomes considerably thinner, about $0.02 \times r_{shock}$, in the moving medium stage. This is a feature predicted by the self-similar solution. The expansion rate of the contact discontinuity as a function of time is shown in Figure 4. Thick solid line represents one-dimensional numerical result while thin solid lines show constant expansion rates, $r \propto t^a$, $a = 2/5, 3/5, 1, 6/5$ from the flattest to the steepest curve for comparison. At the end of the simulation, the expansion rate of the contact discontinuity reaches about $a = 1.189$ which is close to the predicted value by the self-similar solution for the constant luminosity and uniform ejecta density. Recall that the expansion rate derived in the self-similar solution for varying luminosity and power law density profile is $r \propto t^a$, $a = \frac{6-n-l}{5-n}$, where n is the power law index of the ejecta density profile ($\rho \propto r^{-n}$) and l is the power law index for the pulsar luminosity ($L \propto t^{-l}$). We find that the time scale for the system to reach the self-similar stage is sensitive to the physical variables such as the pulsar wind and background ejecta flow. The system evolves faster for the higher pulsar luminosity but slower for the higher supernova ejecta density. Also, the evolution takes shorter time for higher ejecta velocity and higher density of pulsar wind gas for a given luminosity. The faster evolution for the higher density of pulsar wind in a given pulsar luminosity is likely because the higher momentum is allowed by choosing a higher density for a given luminosity (recall that the pulsar mechanical luminosity is $L = 2.0 \times \pi r^2 \rho v^3$).

4.2. Hydrodynamic Instabilities : Two-Dimensional Numerical Simulation

Numerically, we found three independent instabilities in the interaction region between the pulsar wind and the supernova ejecta. The first weak instability occurs in the very beginning, and is caused by the impulsive acceleration of dense ejecta by the low density pulsar wind. But this is a very weak instability and does not grow significantly at the interface (see Fig.5a). The second instability develops in the post-shock flow during the intermediate stage (Fig.5b). This second instability develops briefly while the gradients of density and pressure are of opposite signs (satisfying the criterion of the R-T instability). This unstable flow develops in the transition between the stationary medium stage (Weaver’s self-similar stage) and the moving medium stage (Chevalier’s self-similar stage). In the stationary medium stage, both pressure and density profiles in the post-shock region show positive gradients (see Fig.3a). On the other hand, in the moving medium stage, both pressure and density in the post-shock region show negative gradients (see Fig. 3c). In each stage, the post-shock flow is stable. However, while the stationary medium stage evolves into the the moving medium stage, the postshock pressure and density evolve by $P \propto v^2 t^{-3}$ and $\rho \propto t^{-3}$, respectively. Therefore, the pressure decreases more rapidly with time than the density if the power law index of the shock expansion ($r \propto t^a$) is smaller than 1.0. The different evolutions of density and pressure result in the unstable flow that shows a positive gradient in density profile but a negative gradient in pressure profile (see Fig.3b). This unstable flow disappears when the shock expansion accelerates. Small fingers in Figure 5b are the results of this second instability. We note that the fingers are confined within the shell and the outer shock front is not affected by this instability. The first and second instabilities do not result in the formation of significant long filaments but they play a role as seed perturbation for next strong instability.

The third and most important instability develops in the contact discontinuity between

the pulsar wind and the shocked supernova ejecta as the pulsar bubble becomes accelerated ($r \propto t^a, a > 1.0$). This is the strongest instability and produces pronounced filamentary structures (Fig. 6). The thin layer between the shock and the contact discontinuity is severely distorted because of the instability (note that the shock front is not affected by the first and second instabilities). Figure 6 shows a number of thin fingers pointing toward the center. At later times, most of these thin fingers become unstable while some fingers maintain their stability longer. Some unstable fingers are found to be detached from the shell. The disruption of long thin fingers is caused by a secondary Kelvin-Helmholtz (K-H) instability that develops along the shear layer between the pulsar’s low density nebula and the R-T finger. The growth rate of the K-H instability decreases as the relative density ratio between two gases increases. The formation of these stable long fingers is possible because of the large density difference between the shocked thin layer and the low density pulsar bubble. Therefore, fingers will be able to maintain their stable long structure for longer evolution if the density in the pulsar nebula is lower. Actually, this is what we expect to happen in the Crab Nebula. The stability of fingers should be also affected by the strong magnetic field in the Crab Nebula (Hester et al. 1996).

As the R-T fingers grow, the mixing layer becomes thicker at later times. The normalized thickness of the mixing layer is expected to increase with time as long as the shell acceleration goes on. The angle-averaged density of two-dimensional numerical simulation at $t = 4000$ years is compared to the one-dimensional result in Figure 7. The shell becomes much thicker and the average density in the shell is decreased as results of mixing in two-dimensional numerical simulation compared to the one-dimensional result.

What is most noticeable is the formation of dense heads on the R-T fingers, which can be compared to regions F or G in the HST image of Hester et al. (1996). These dense finger heads are attributed to the compressibility of the gas. The density in dense finger heads

is found to be about 10 times higher than in other regions of the fingers. The density is expected to increase if the cooling is important. The general morphology of our numerical results is compared to the HST observation of the filaments in the Crab Nebula (see Hester et al. 1996) and found to resemble the observations.

5. Mass and Acceleration of R-T fingers

Figure 8 shows the mass distribution of the shocked supernova ejecta as functions of radius (left column) and density (right column). The histograms in the left panels illustrate the mass distribution contained within a shell bounded by two radii (r_1, r_2). The mass is normalized by total mass. The radius is also normalized by the outer boundary of the computational plane. Recall that the outer boundary in the r-direction expands with the shock velocity and the shock front is distorted because of the strong instability. The right panels show the normalized mass distribution as a function of the density normalized by the unshocked ejecta density. The mass distribution of shocked supernova material extends farther inside with an increasing evolution time as seen from top panel ($t=1000$ years) to bottom panel ($t=4000$ years) due to the growth of R-T fingers. Also, the higher density fingers are found to form at later times (compare the mass distributions as a function of density at 1000 years and 2000 years or later). This result confirms that the high density at the tip of R-T finger is actually generated by the compressible flow pouring down to the fingers from the shell rather than simple drifting material from the shell.

The total mass in the shell changes with time as the supernova material flows in from the outer shock and some mass drains away through the formation of the R-T fingers. Table 1 shows the relative amount of mass and kinetic energy confined within the shell and R-T fingers at a given time. The mass is normalized by the total shocked supernova mass. The thickness of the shell approaches to about $0.02 \times r_{shock}$ in the self-similar stage ($r \propto r^{1.2}$)

where r_{shock} is the radius of outer shock. Our two-dimensional numerical solution shows that the outer shock is severely distorted by the instability and the thickness of thin shell varies as a function of azimuthal angle. In order to estimate the mass within the shell approximately, we first take the shell thickness as $0.02 \times r_{shock}(\phi)$ where $r_{shock}(\phi)$ is the shock radius at ϕ . As a comparison, we also listed each mass in the shell and the R-T fingers by taking the shell thickness as $0.03 \times r_{shock}$ in Table 1(b). Our results show that the relative mass amount in the shell decreases from $t=1000$ years to $t=2000$ years and then increases later. This is because the R-T fingers, due to the acceleration, are not fully grown and small R-T fingers still exist close to the shell. Besides, the shell thickness at $t=1000$ years is greater than $0.02 \times r_{shock}$. By looking at the trend from $t=2000$ years to $t=4000$ years, we can see that the relative mass in the shell increases with time while the relative mass in R-T fingers decreases. This means that incoming mass flux from the outer shock is larger than outgoing mass flux through the formation of R-T fingers. Once the long R-T fingers are fully developed, the mass confined in R-T fingers is roughly about 60% – 75% of total shocked mass and larger than contained in the shell (25% – 40%). Kinetic energy also shows a similar tendency to the mass. Considering kinetic energy change only between $t=2000$ yrs and $t=4000$ yrs, about 55% – 72% of total shocked kinetic energy is in the R-T fingers and 28% – 45% is in the shell. Also, the kinetic energy in the shell increases with time while the kinetic energy in the R-T fingers decreases with time. The slightly higher percentage of kinetic energy in the shell than mass can be explained because the flow velocity in the shell is higher than the velocity of the R-T finger.

Figure 9 shows the power law indices of expansions of R-T fingers and forward shock front for the different periods of time. The radius of R-T fingers is measured at the tip of the fingers. This point is detected by averaging the mass fraction function and taking the location where the angle-averaged mass fraction is 0.01 (recall that the mass fraction in the pulsar wind was 0.0 and the supernova ejecta material had mass fraction 1.0 in the

beginning). First of all, the expansion rates for both R-T fingers and shock front increase with time. After about $t=1000$ years, both the R-T fingers and shock front start to accelerate, but the shock front achieves a higher expansion rate than the R-T fingers. The expansion of the R-T fingers reaches an asymptotic limit at about $a = 1.04$ to 1.05 ($r \propto t^a$). This expansion rate is a little higher than the free expansion. In earlier stage ($t=100 - 500$ yrs), the expansion rates of R-T fingers and shock front are close to each other because the R-T instability is not fully developed. Once the R-T fingers grow due to the instability, they are decoupled from the shell and they experience smaller acceleration than the thin shell. On the other hand, the shock front keeps accelerating until the expansion rate reaches the self-similar value ($a=1.2$). In our simulation, the power law index for the shock front expansion reached about 1.157 during $t=3000 - 4000$ yrs. We expect that the power law index of the expansion rate of the shock front will reach its self-similar value as we evolve the system further. This result tells us about the important history of R-T fingers. The supernova material is first accelerated impulsively by the pulsar wind and decelerates until the expansion of thin shell between the contact discontinuity and the forward shock starts to accelerate as the system approaches the self-similar stage. Once the thin shell accelerates, the R-T instability develops and the R-T fingers experience less acceleration by decoupling from the shell and falling down along the effective gravity vector. According to our numerical results, we can infer that the accelerated filaments in the Crab nebula should have been accelerated more efficiently right before the R-T fingers were not completely decoupled from the thin shell. We will discuss this issue further in the next section.

6. Application to the Crab Nebula and Discussion

Our simulation is simple in terms of relevant physics and initial condition. For example, we have not considered the effect of magnetic field and radiative cooling. Strong magnetic

field is known to affect the stability and growth of R-T fingers (see Jun, Norman, and Stone 1995). We expect that inclusion of magnetic field in our numerical simulation may generate more stable long fingers since the secondary K-H instability can be suppressed by the magnetic field. Also, tangential magnetic field may enhance coupling between the thin shell and the R-T fingers and slow down the inward velocity of the R-T finger. As a result, the expansion power law index of the R-T fingers may be increased. Radiative cooling is expected to increase the density in thin shell and R-T fingers and to affect the growth of R-T instability. The cooling process may change the mass distribution of the shocked supernova ejecta. Therefore, the inclusion of magnetic field and radiative cooling in the model is important in order to explain the detailed structure of the filaments. Besides, due to the lack of good information about initial conditions such as the pulsar wind, the exact quantitative comparison to the Crab Nebula should not be made at the moment. Nevertheless, some qualitative results can be applied to understand the Crab Nebula better.

Bietenholz et al. (1991) found that the synchrotron component of the Crab Nebula has accelerated since the supernova explosion and the acceleration of the synchrotron component may be larger than that of the emission-line filaments. This observation is explained well by our numerical simulation since the forward shock front and thin shell accelerates with a higher rate than the R-T fingers. From the table 2 in Bietenholz et al. (1991), we can derive the power law index of the expansion for the outer edge of the synchrotron nebula because the observations were carried out in two different years, 1982, 1987. Using the relation for the expansion power law index, $a = \frac{\log(r_1/r_2)}{\log(t_1/t_2)}$ where r_1 and r_2 are the radii at two different ages, t_1 and t_2 , we calculate the expansion power law index, $a = 1.245 \sim 1.328$. This power law index is somewhat larger than the predicted (1.2) from the self-similar solution for the constant luminosity and uniform ejecta density. The discrepancy could have two possible origins. First, the observed expansion parameter in Bietenholz et al. (1991) is only an approximate value because of the difficulty in comparing

two radio images. Also, the exact date of the observations used can change the result. Second, the density in the supernova ejecta may be a decreasing function of the radius. For example, the self-similar solution predicts the power law index to be 1.25 for the power law index of the ejecta density of 1.0 and constant pulsar luminosity. In order to calculate the expansion power law index for the emission-line filaments, we use Trimble’s result of the convergence date, $t = 1140$ yrs, using two sets of data in 1950 and 1966. Therefore we can derive the expansion parameter, $e = 0.9806$ using the relation, $t_e = \delta t / (1 - e)$ (see Bietenholz et al. 1991). And we calculate the expansion power law index, $a = 1.107$. This value is also larger than our numerical result, $a = 1.04 \sim 1.05$. In general, the observed expansion power law indices of synchrotron nebula and filaments are reasonably close to our numerical simulation. This is an encouraging result which supports the current model for the Crab Nebula. More accurate future observations of the expansion rate of each component are highly desirable.

With two known expansion power law indices, we can derive when the R-T instability due to the acceleration began to develop in the Crab Nebula. We assume that the expansion rate has been constant since the development of the R-T instability. We can now write a relation among the length of the R-T finger, an initial time of the R-T instability development, and the expansion power law indices (a_f for the filaments and a_s for the shock front) of the R-T fingers.

$$\frac{\delta r}{r_s} = 1 - (t/t_0)^{a_f - a_s} \quad (14)$$

where δr is the length of the R-T finger, r_s is the radius of the forward shock front, t is the current age of the Crab Nebula, and t_0 is the initial time of the R-T instability development. Now let’s use Hester’s observation to obtain the length of the R-T finger. By choosing the regions F or G in the Figure 1 of Hester et al. (1996), we take the length of the R-T finger as about 0.2 times the radius of the forward shock front. Here we also assume that the shock front is located near the top of the R-T finger and we use the expansion power law

index for the outer edge of the Crab Nebula as the expansion power law index for the shock front. Then we derive the initial age of the R-T instability development at the regions F or G, $t_0 = 266$ years. This means that the R-T fingers in region F or G began growing 657 years ago. This is an interesting result with regard to the history of the line-emitting filaments. The filaments in the Crab Nebula started to form around the age of 266 years and the acceleration of the filaments should have been strongest at that time. We should note that this initial time for the R-T instability is an approximate estimate because of our assumptions including constant pulsar luminosity. Other smaller fingers in regions D imply two different interpretations for the timescale of the formation. First, those fingers may have started developing more recently compared to the fingers in regions F or G if the shell in region D experiences same expansion rate as region F or G. Second, if the fingers in region D have developed at the same time as regions F or G, then the expansion rate, that is acceleration of the shell, must have been slower in that region than region F or G. This spherically asymmetric expansion rate could be caused by the asymmetric pulsar wind. Observational measurements of expansion rate in different azimuthal regions is required to check these ideas. One also needs to remember that we have not considered the effect of magnetic fields in controlling the growth of the R-T fingers. Our simulation cannot explain long large filamentary structures extending continuously from the 'skin' to near the center. We speculate that these structures could be formed as the pulsar's wind sweeps the supernova ejecta which contain large degree of inhomogeneity in density.

7. Conclusions

Our numerical simulation of the interacting pulsar bubble with expanding supernova ejecta produces well-developed filamentary structures which resemble the filaments in the Crab Nebula. Three instabilities are found to develop independently in different

evolutionary stages. The first weak instability develops near the contact discontinuity at early stage of the evolution due to the impulsive acceleration of the dense ejecta by the pulsar wind. The second instability develops within the postshock flow region between the shock front and the contact discontinuity. The second instability is a time-transient phenomenon before the system develops into the self-similar flow. The third Rayleigh-Taylor instability driven by the acceleration of the thin shell which develops in the later stage is found to be the strongest and provide a main mechanism for the origin of the filaments.

As a result of the third R-T instability, the forward shock front is severely distorted, while the first two instabilities could not disturb the shock front. A number of long R-T fingers are generated by the instability and these fingers become unstable (Kelvin-Helmholtz instability) due to the relative motion between the fingers and background flow. However, the development of the K-H instability can be delayed by a higher density ratio between two fluids and strong magnetic field. The fingers produce dense heads at their tips and these dense finger heads are attributed to the compressibility of the gas. The density of these heads is about 10 times higher than other parts of the fingers and expected to increase in the presence of the cooling effect. After the long R-T fingers are fully developed, the mass contained in the R-T fingers is found to be roughly 60% – 75% of the total shocked mass. Kinetic energy within the R-T fingers is about 55% – 72% of the total kinetic energy in the shocked flow. The R-T fingers are found to accelerate with a slower rate than the shock front as they are decoupled from the shell. In our simulation, the expansion power law index (α) for the tip of R-T fingers is about $1.04 \sim 1.05$ while the index for the shell is about 1.157. These results are close to the observed values in the Crab Nebula (1.107 for the line-filaments and $1.245 \sim 1.328$ for the outer edge of the synchrotron nebula). The small difference between our numerical results and the observations could be improved if the expanding supernova ejecta has the density profile of $\rho \propto r^{-1}$ or r^{-2} . Considering the different expansion rates between the outer edge of the synchrotron nebula and the

line-emitting filaments, we can infer that the several long fingers (region F or G in Hester’s observation) in the Crab Nebula started to grow about 657 years ago.

In summary, our model can explain important observational features of the Crab Nebula. They are the accelerations of the filaments and the synchrotron nebula, formation of thin skin connecting the filaments, formation of the filaments pointing toward the center, and high-density finger heads.

I am grateful to Roger Chevalier, Jeff Hester, Tom Jones, Mike Norman, and Jim Stone for useful discussion and encouragement. The work reported here is supported by NSF grant AST-9318959 and by the Minnesota Supercomputer Institute.

REFERENCES

- Bietenholtz, M.F. & Kronberg, P.P. 1990, ApJ, 357, L13
- Bietenholz, M.F., Kronberg, P.P., Hogg, D.E., & Wilson, A.S. 1991, ApJ, 373, L59
- Bietenholtz, M.F., Kassim, N., Frail, D.A., Perley, R.A., Erickson, W.C., & Hajian, A.R.
1997, preprint
- Chevalier, R.A. & Gull, T.R. 1975, ApJ, 200, 399
- Chevalier, R.A. 1977, in Supernovae, ed. D.N. Schramm (Dordrecht: Reidel), 53
- Chevalier, R.A. 1984, ApJ, 280, 797
- Chevalier, R.A. & Fransson C. 1992, ApJ, 395, 540
- Clarke, D. A. & Norman, M. L. 1994, NCSA Tech Report 15,
<http://zeus.ncsa.uiuc.edu:8080/lca/zeus3d/zeus32.ps>.
- Davidson, K. & Fesen, R.A. 1985, ARA&A, 23, 119
- Frail, D.A., Kassim, N.E., Cornwell, T.J., & Goss, W.M. 1995, ApJ, 454, L129
- Hester, J.J. et al. 1996, ApJ, 456, 225
- Jun, B.-I., Norman, M.L., & Stone, J.M. 1995, ApJ, 453,332
- Jun, B.-I. 1997, in Proceedings of the 12th 'Kingston meeting' on Theoretical Astrophysics:
Computational Astrophysics (ASP Conference Series, 123), eds. D.A. Clarke & M.J.
West, (San Francisco: ASP), 94
- Jun, B.-I. & Norman, M.L. 1996, ApJ, 465, 800
- Jun, B.-I. & Norman, M.L. 1996, ApJ, 472, 245

Kennel, C.F. & Coroniti, F.V. 1984, ApJ, 283, 694

Rees, M.J. & Gunn, J.E. 1974, MNRAS, 167, 1

Sankrit, R. & Hester, J.J. 1997, ApJ, submitted

Stone, J.M. & Norman, M.L. 1992, ApJS, 80, 753

Trimble, V.L. 1968, AJ, 73, 535

Weaver, R., McCray, R., Castor, P.R., & Moore, R.T. 1977, ApJ, 218, 377

Fig. 1.— Schematic representation of the normal type-II supernova remnant model for the simulation. The figure shows the pulsar wind blowing into the uniformly expanding supernova remnant. The pulsar is located in the center. The small dotted circle outside of the pulsar is the wind termination shock. This shock heats up the wind gas and produces a hot bubble expanding into the supernova remnant. The contact discontinuity between the pulsar bubble and the shocked supernova gas is shown to be Rayleigh-Taylor unstable. The R-T fingers are connected to each other by a thin shell confined by the forward shock. Note that this forward shock front is actually distorted by the development of the instability in the numerical simulation (see Fig.6). Outside the forward shock, there are expanding supernova ejecta, reverse shock, and blast wave of the supernova.

Fig. 2.— Self-similar solutions for the model described in Fig.1. D, P, and V represent the density, gas pressure, and the velocity, respectively. Each plot shows the physical variables in the region between the contact discontinuity and the shock front ($\zeta = 1$).

Fig. 3.— One-dimensional numerical simulation of the normal type-II supernova remnant model. Fig.3a shows the result at the stationary medium stage. From inside outward, the wind termination shock (W.T.), contact discontinuity (C.D.), and forward shock (F.S.) are seen at the designated location. Each plot in the same column represents the density, velocity, and gas pressure from top to bottom, respectively. Fig.3b and 3c are the results at the intermediate stage and the moving medium stage, respectively (see the text for the detail).

Fig. 4.— The figure plots the radius of the contact discontinuity as a function of time. The thick solid line represents the one-dimensional numerical result while other thin solid lines show constant expansion rate, $r \propto t^a$, $a = 2/5, 3/5, 1, 6/5$ from the lowest to the highest.

Fig. 5.— The first image (left) shows the density of two-dimensional numerical result

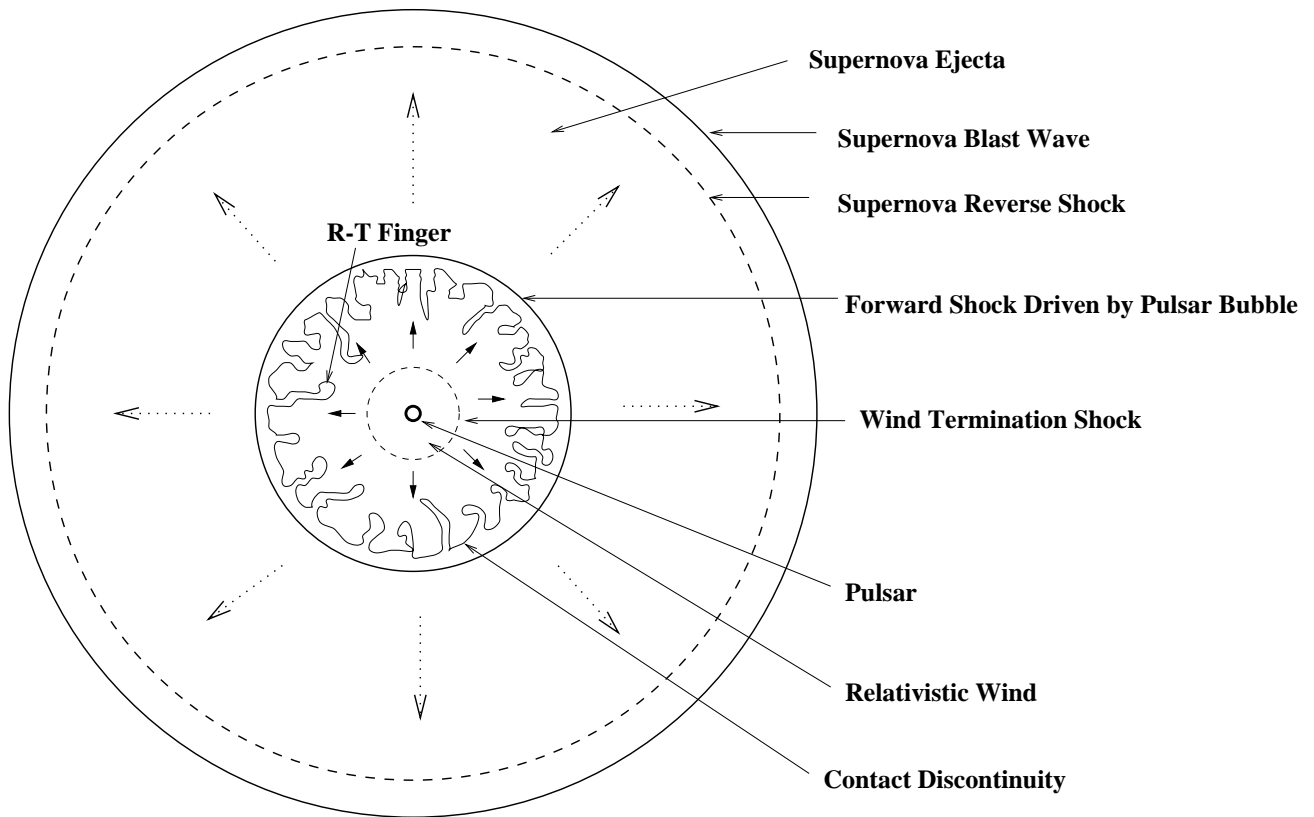
at $t=100$ yrs. From the center, each circle corresponds to the contact discontinuity, the forward shock driven by the pulsar bubble, and computational boundary. The computational boundary is round because the simulation is carried out in the spherical geometry and remapped onto the cartesian grids. The wind termination shock is located inside the contact discontinuity. It is not visible in this image because of low density (see Fig.3). The development of a very weak instability near the contact discontinuity is seen. The right image shows the result at $t=600$ yrs. The forward shock is seen near the outer computational boundary. A number of small fingers are developed in the postshock flow because of the R-T instability in the flow. Lighter color represents higher density.

Fig. 6.— The density images of two-dimensional numerical simulation at $t=1000$ (Fig.6a), 2000 (Fig.6b), 3000 (Fig.6c), 4000 (Fig.6d) yrs. Note that the forward shock front is always located near the outer computational boundary because the grid is moving with the shock velocity. Lighter color represents higher density.

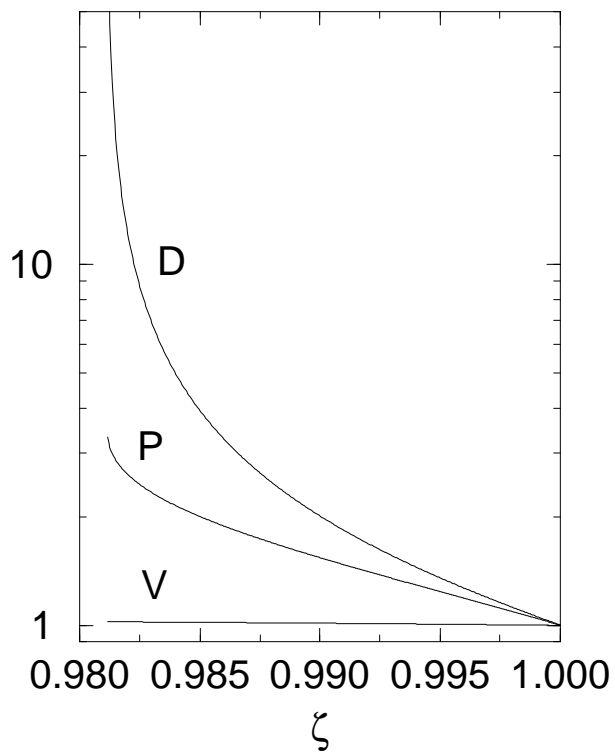
Fig. 7.— The comparison between one-dimensional numerical result and two-dimensional result at $t=4000$ yrs. Two-dimensional result is averaged along the angle-direction.

Fig. 8.— Mass distribution of the shocked supernova ejecta as a function of radius (left plots) and density (right plots). Each plot corresponds to the mass distribution at $t=1000$, 2000, 3000, and 4000 yrs from top to bottom.

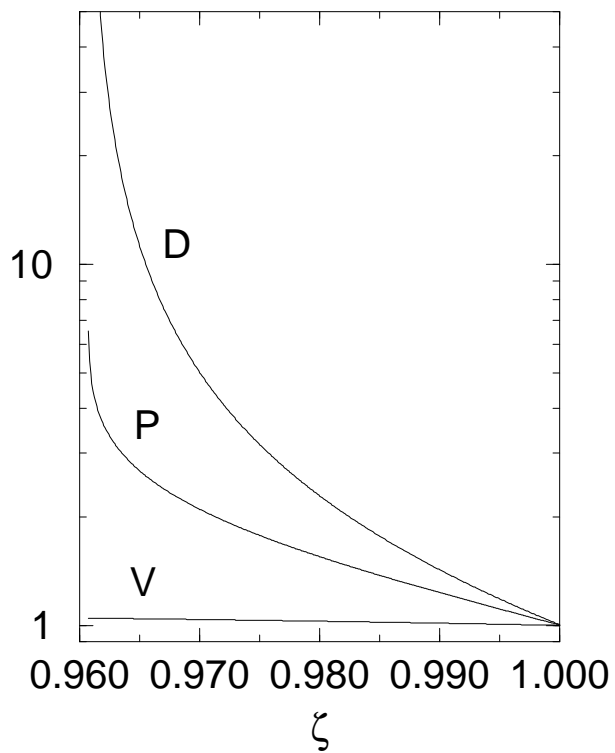
Fig. 9.— The expansion rate of the R-T fingers and shock front as function of different period of time. The figure plots power law index of expansion, $a = \frac{\log(r_1/r_2)}{\log(t_1/t_2)}$. The power law indices for the shock front and the R-T fingers are represented by circles and rectangles, respectively.



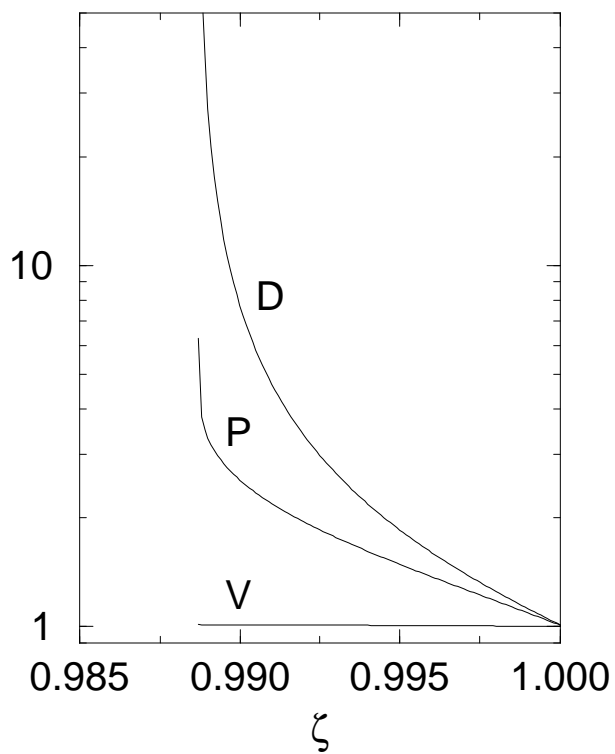
(a) $n = 0, l = 0, a = 1.2, \gamma = 5/3$



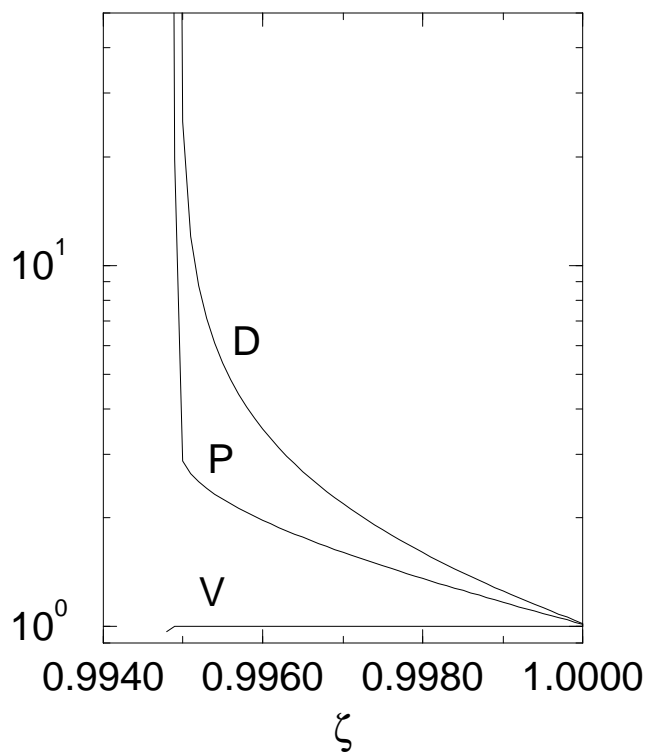
(b) $n = 3, l = 0, a = 1.5, \gamma = 5/3$



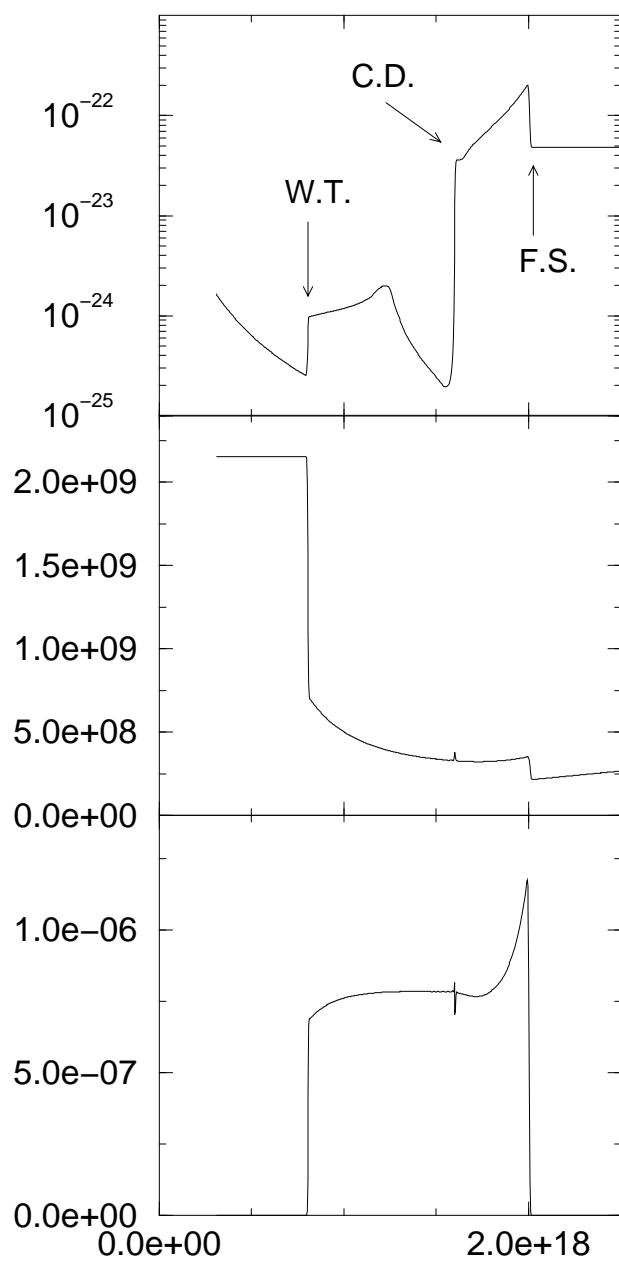
(c) $n = 0, l = 0.5, a = 1.1, \gamma = 5/3$



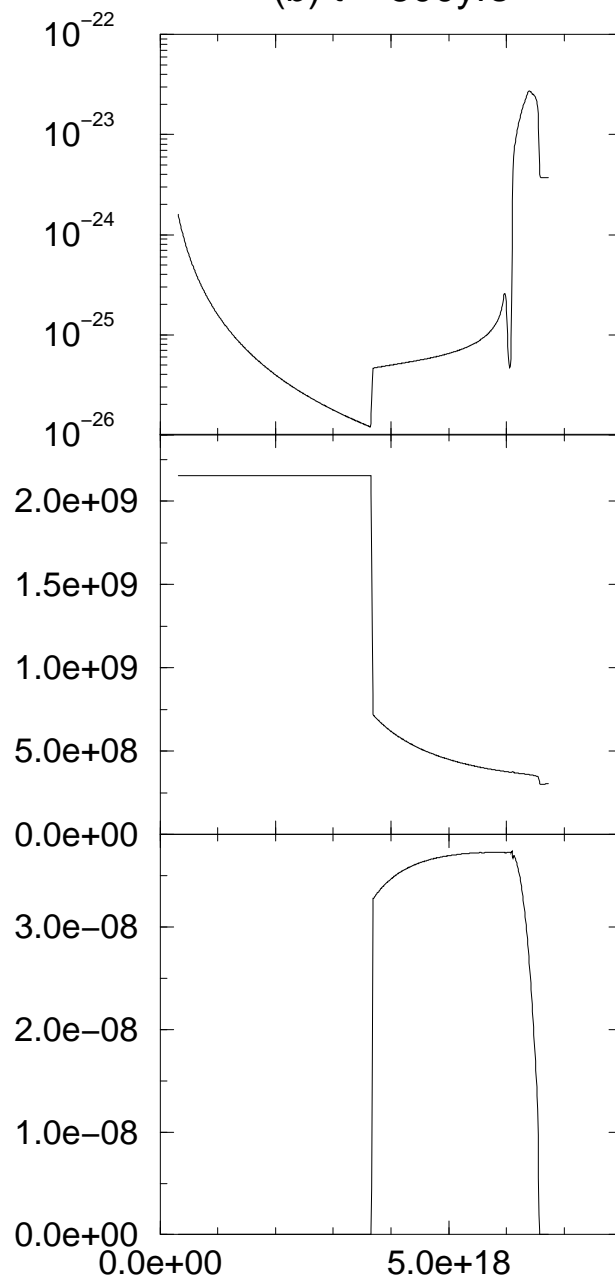
(d) $n = 0, l = 0, a = 1.2, \gamma = 1.1$



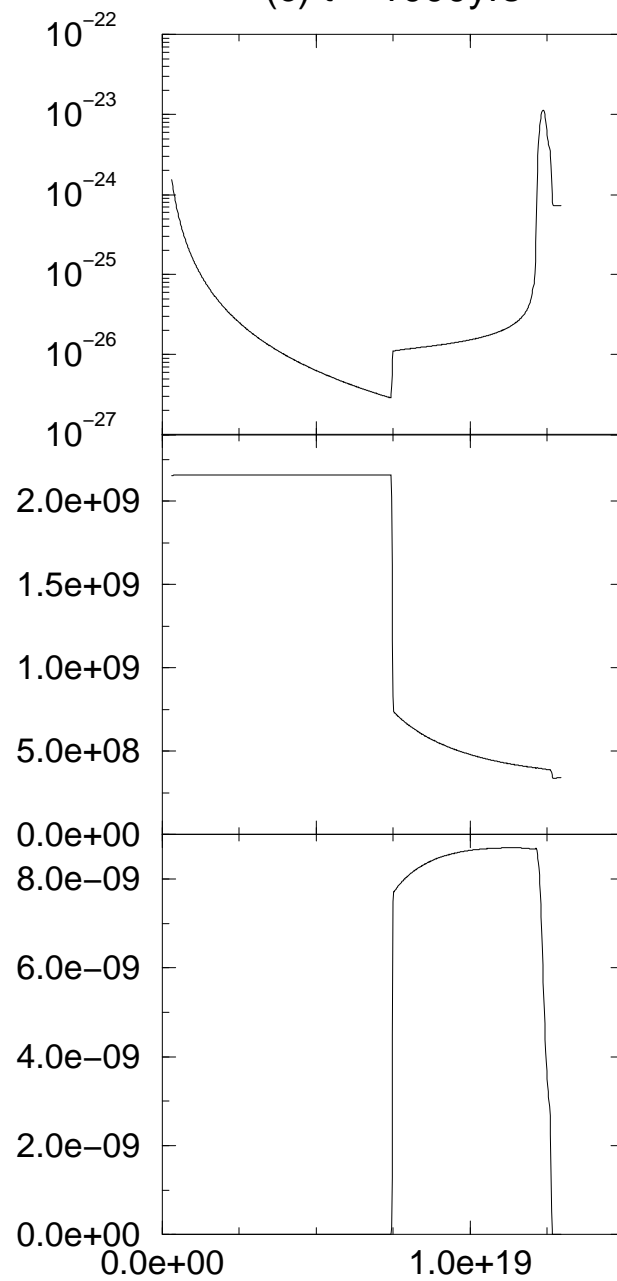
(a) $t = 100\text{yrs}$

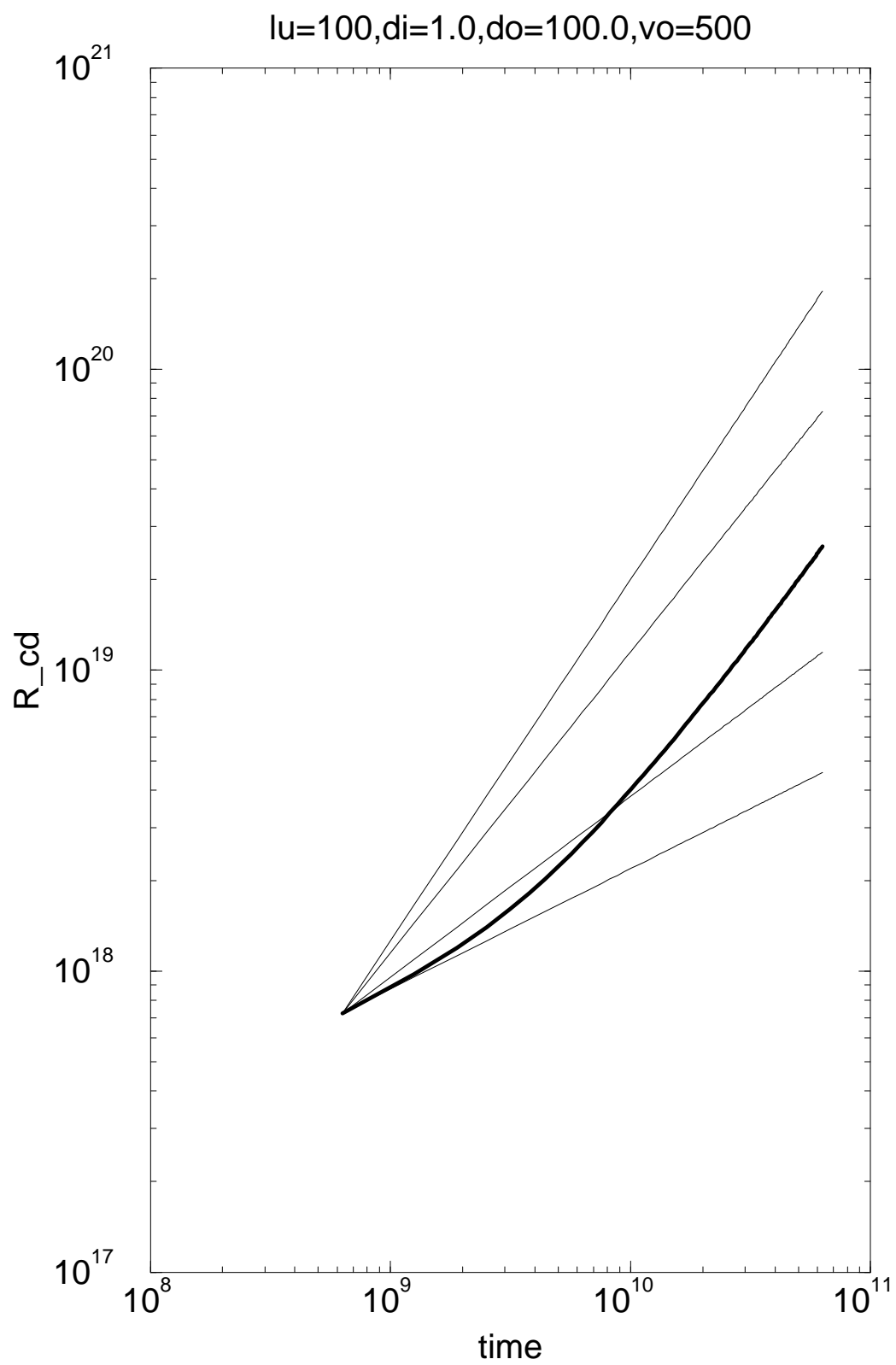


(b) $t = 500\text{yrs}$

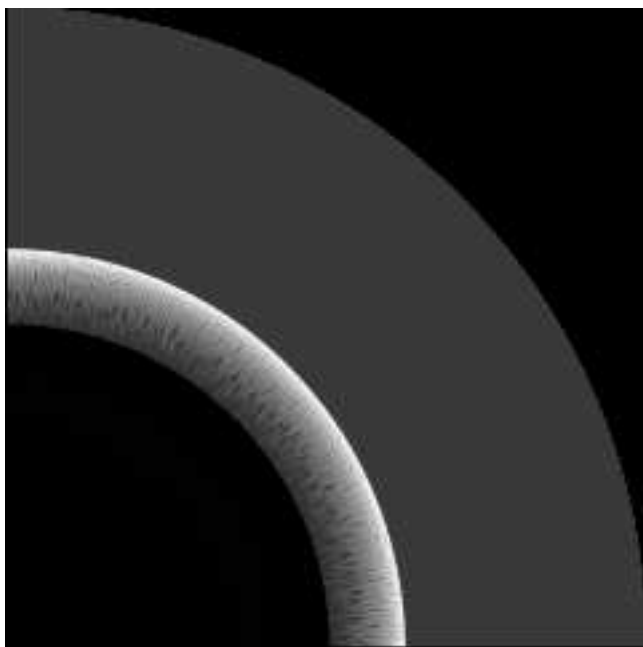


(c) $t = 1000\text{yrs}$

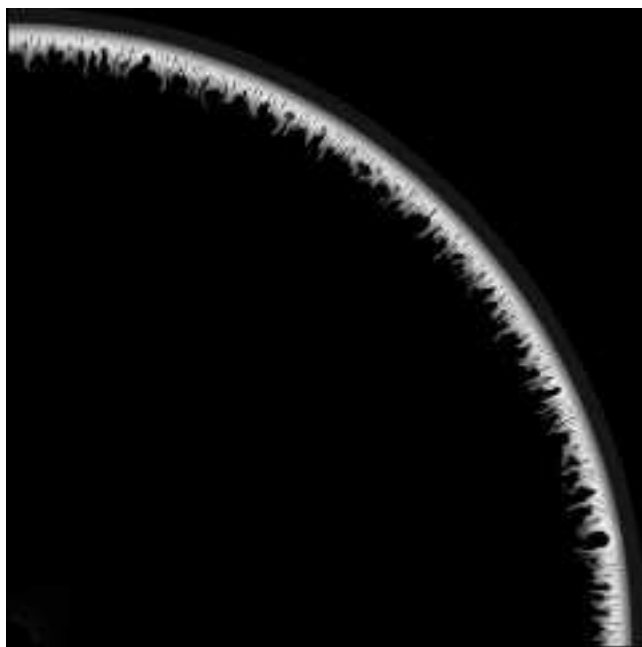




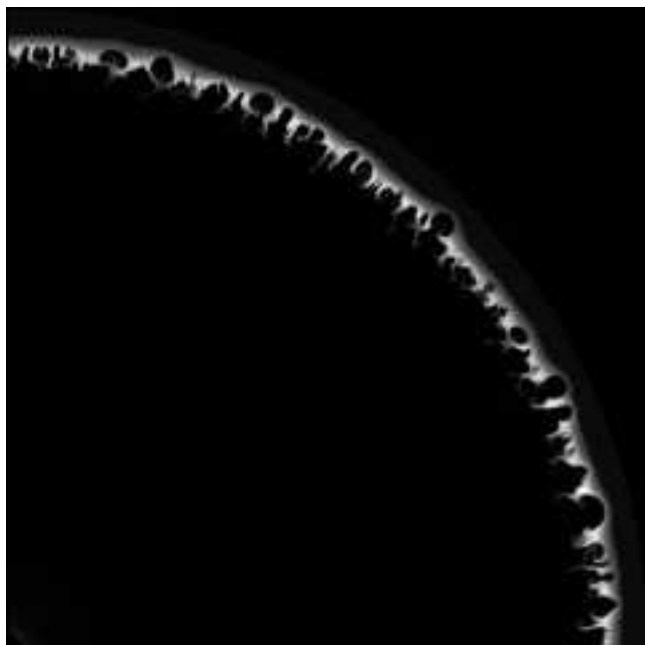
(a)



(b)



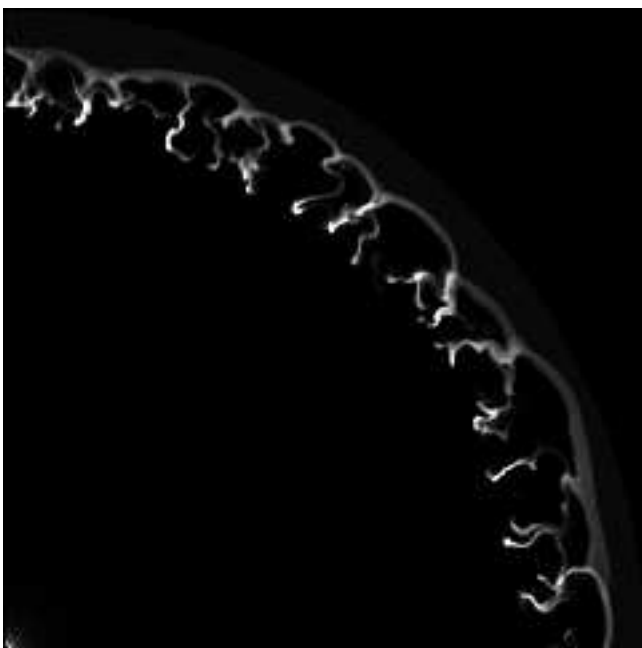
(a)



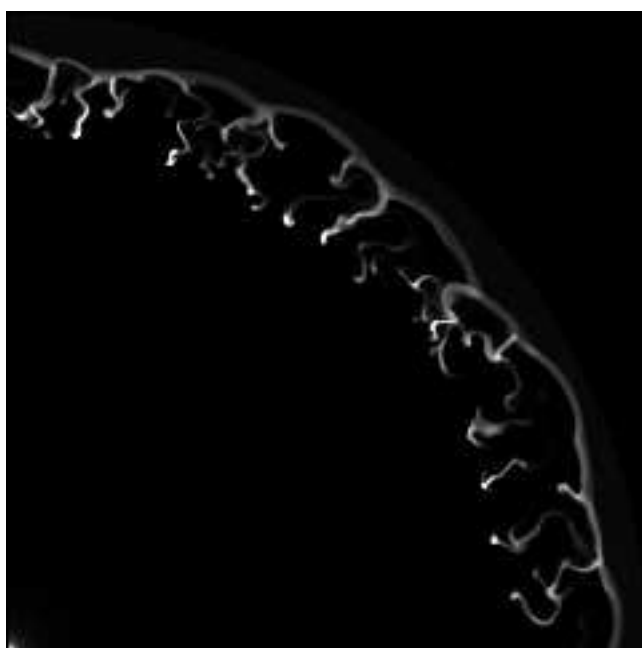
(b)

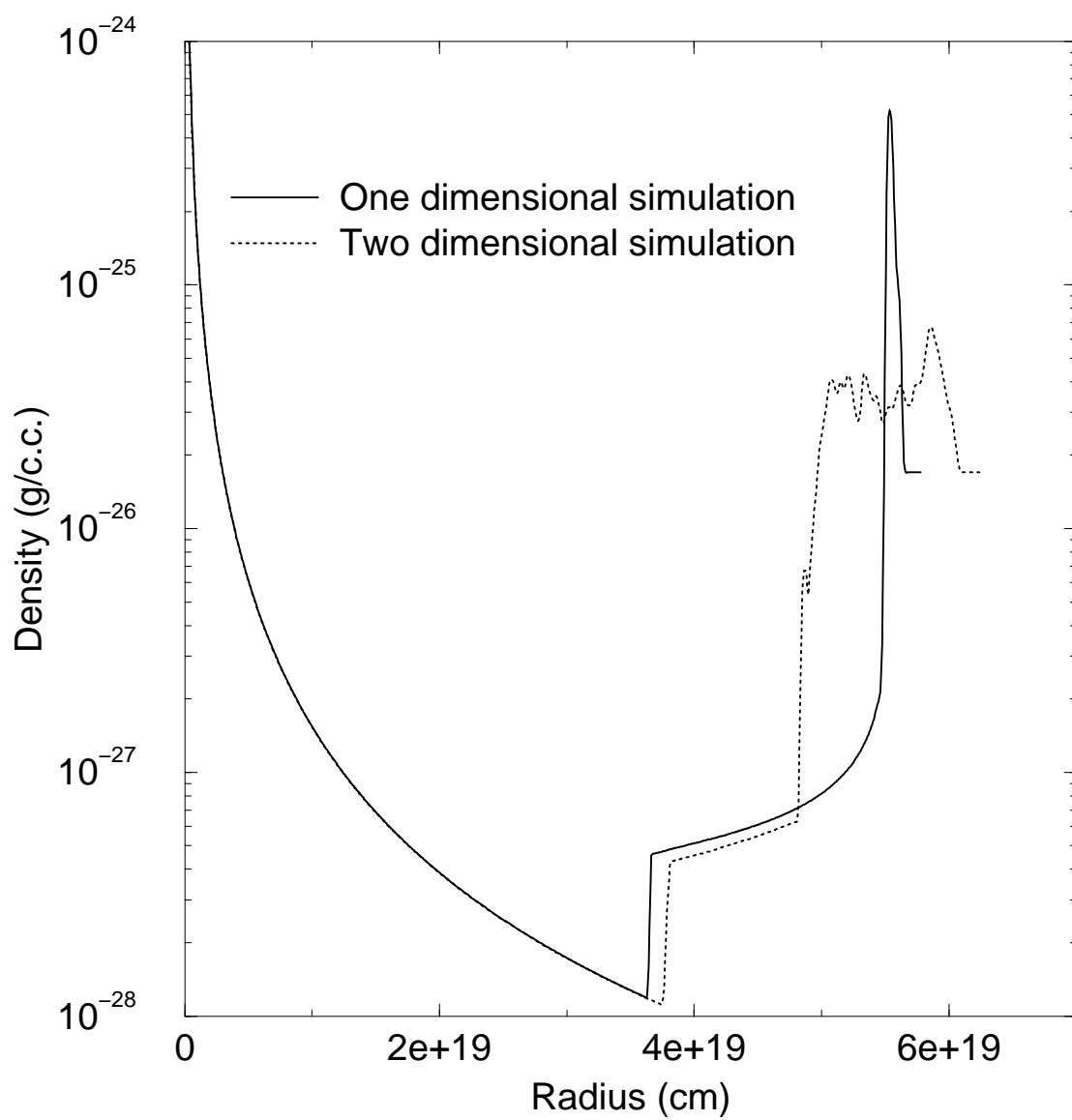


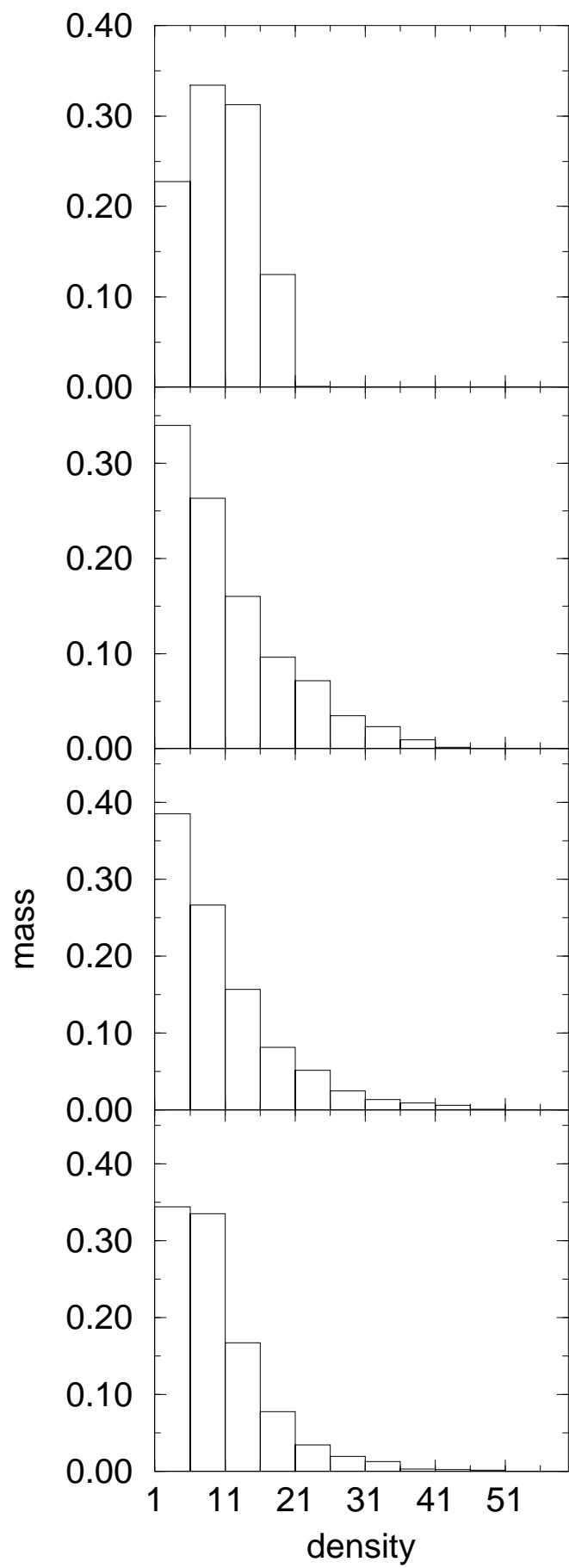
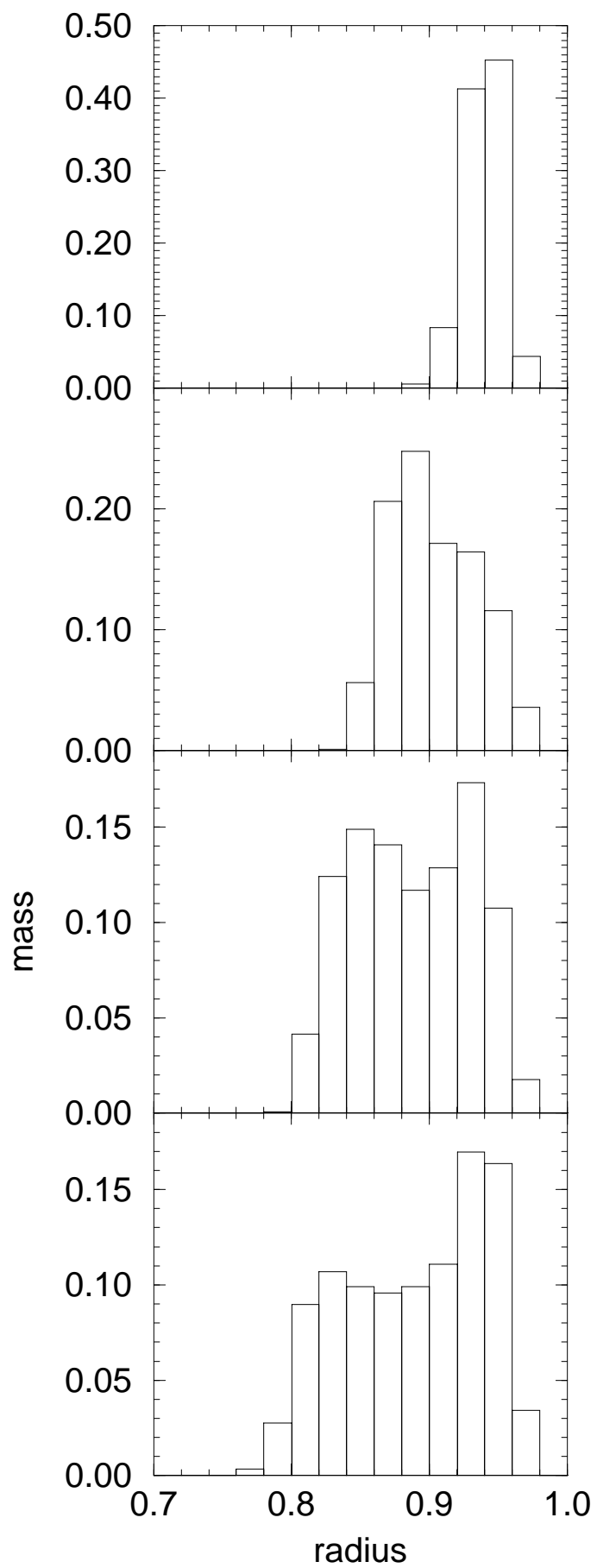
(c)



(d)







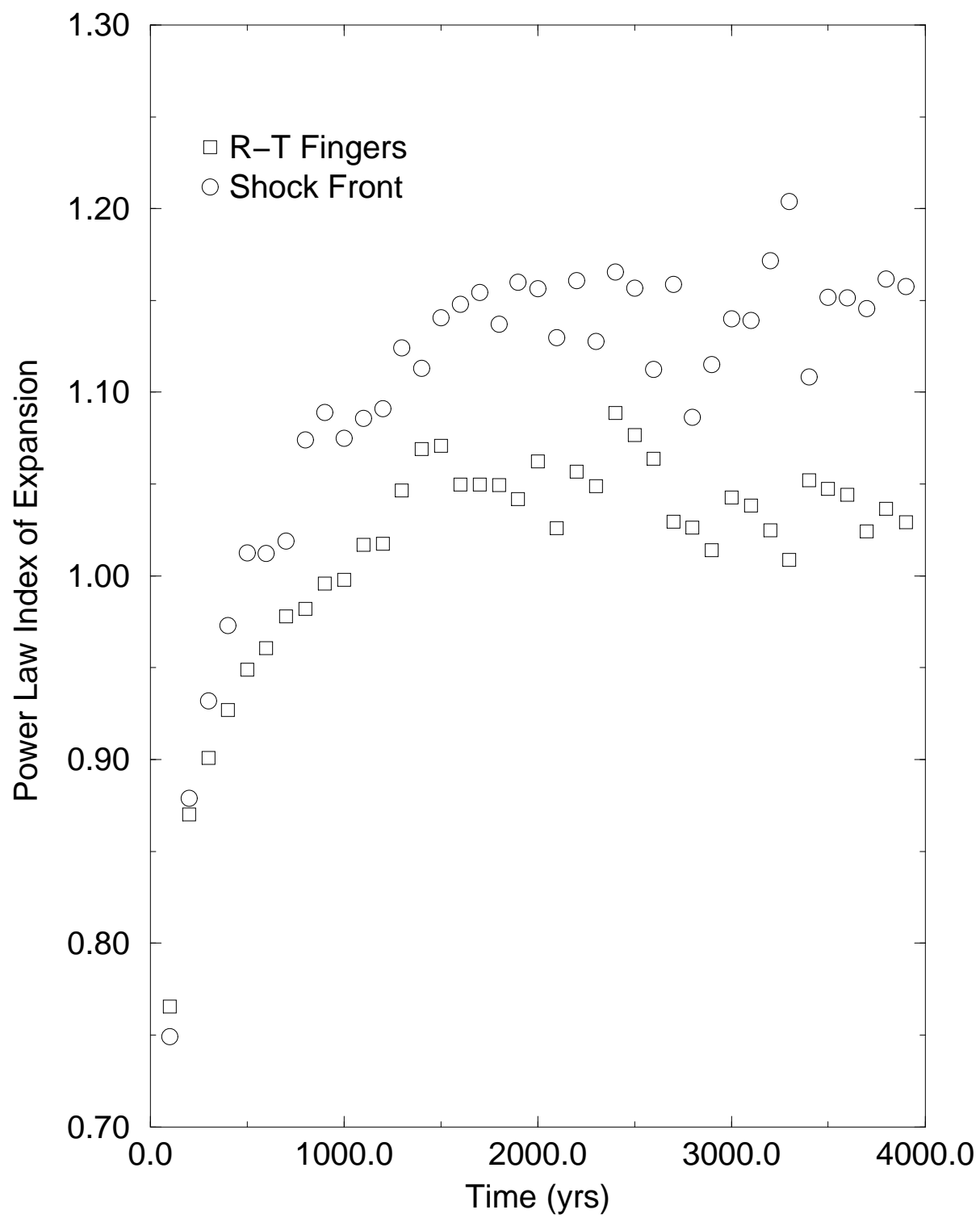


Table 1. Mss and Kinetic Energy in a thin shell and R-T fingers(a) Thickness of thin shell = $0.02r_{shock}$

Years	M_{shell}	$M_{fingers}$	E_{shell}	$E_{fingers}$
1000	35.8 %	64.2 %	36.7 %	63.3 %
2000	24.9 %	75.1 %	28.0 %	72.0 %
3000	27.0 %	73.0 %	30.8 %	69.2 %
4000	32.2 %	67.8 %	37.4 %	62.6 %

(b) Thickness of thin shell = $0.03r_{shock}$

Years	M_{shell}	$M_{fingers}$	E_{shell}	$E_{fingers}$
1000	62.8 %	37.2 %	63.8 %	36.3 %
2000	32.5 %	67.5 %	36.1 %	63.9 %
3000	35.1 %	64.9 %	39.5 %	60.5 %
4000	38.4 %	61.6 %	44.3 %	55.7 %